

LJMU Research Online

Ortega Martorell, S, Candiota, AP, Thomson, R, Riley, P, Julia-Sape, M and Olier-Caparroso, I

Embedding MRI information into MRSI data source extraction improves brain tumour delineation in animal models

http://researchonline.ljmu.ac.uk/id/eprint/11142/

Article

Citation (please note it is advisable to refer to the publisher's version if you intend to cite from this work)

Ortega Martorell, S, Candiota, AP, Thomson, R, Riley, P, Julia-Sape, M and Olier-Caparroso, I Embedding MRI information into MRSI data source extraction improves brain tumour delineation in animal models. PLoS One. ISSN 1932-6203 (Accepted)

LJMU has developed LJMU Research Online for users to access the research output of the University more effectively. Copyright © and Moral Rights for the papers on this site are retained by the individual authors and/or other copyright owners. Users may download and/or print one copy of any article(s) in LJMU Research Online to facilitate their private study or for non-commercial research. You may not engage in further distribution of the material or use it for any profit-making activities or any commercial gain.

The version presented here may differ from the published version or from the version of the record. Please see the repository URL above for details on accessing the published version and note that access may require a subscription.

For more information please contact researchonline@ljmu.ac.uk

http://researchonline.ljmu.ac.uk/

1	Embedding MRI information into MRSI data source extraction
2	improves brain tumour delineation in animal models
3	
4	Authors and affiliations:
5	Sandra Ortega-Martorell ^{1,2,*} ; Ana Paula Candiota ^{2,3,4} ; Ryan Thomson ¹ ; Patrick Riley ¹ ; Margarida Julia-
6	Sape ^{2,3,4} ; Ivan Olier ¹ .
7	
8	¹ Department of Applied Mathematics, Liverpool John Moores University, Liverpool, UK
9	² Centro de Investigación Biomédica en Red en Bioingeniería, Biomateriales y Nanomedicina (CIBER-
10	BBN), Cerdanyola del Vallès, Spain
11	³ Departament de Bioquímica i Biologia Molecular, Unitat de Biociències, Universitat Autònoma de
12	Barcelona, Cerdanyola del Vallès, Spain
13	⁴ Institut de Biotecnologia i de Biomedicina, Universitat Autònoma de Barcelona, Cerdanyola del
14	Vallès, Spain
15	
16	* Corresponding author
17	Email: s.ortegamartorell@ljmu.ac.uk
18	
19	Keywords:
20	Magnetic Resonance (MR); MR spectroscopy (MRS); MR imaging (MRI); MR spectroscopic imaging
21	(MRSI); Glioblastoma; Semi-supervised analysis; Fisher Information metric; Multi-Layer Perceptron;
22	Non-negative Matrix factorisation (NMF); Convex-NMF; Semi-Supervised Source Extraction (SSSE)

23 Abstract

24 Glioblastoma is the most frequent malignant intra-cranial tumour. Magnetic resonance imaging is the 25 modality of choice in diagnosis, aggressiveness assessment, and follow-up. However, there are 26 examples where it lacks diagnostic accuracy. Magnetic resonance spectroscopy enables the 27 identification of molecules present in the tissue, providing a precise metabolomic signature. Previous research shows that combining imaging and spectroscopy information results in more accurate 28 29 outcomes and superior diagnostic value. This study proposes a method to combine them, which builds 30 upon a previous methodology whose main objective is to guide the extraction of sources. To this aim, 31 prior knowledge about class-specific information is integrated into the methodology by setting the 32 metric of a latent variable space where Non-negative Matrix Factorisation is performed. The former 33 methodology, which only used spectroscopy and involved combining spectra from different subjects, 34 was adapted to use selected areas of interest that arise from segmenting the T2-weighted image. Results 35 showed that embedding imaging information into the source extraction (the proposed semi-supervised 36 analysis) improved the quality of the tumour delineation, as compared to those obtained without this 37 information (unsupervised analysis). Both approaches were applied to pre-clinical data, involving 38 thirteen brain tumour-bearing mice, and tested against histopathological data. On results of twenty-eight 39 images, the proposed Semi-Supervised Source Extraction (SSSE) method greatly outperformed the 40 unsupervised one, as well as an alternative semi-supervised approach from the literature, with 41 differences being statistically significant. SSSE has proven successful in the delineation of the tumour, 42 while bringing benefits such as 1) not constricting the metabolomic-based prediction to the image-43 segmented area, 2) ability to deal with signal-to-noise issues, 3) opportunity to answer specific questions 44 by allowing researchers/radiologists define areas of interest that guide the source extraction, 4) creation 45 of an intra-subject model and avoiding contamination from inter-subject overlaps, and 5) extraction of 46 meaningful, good-quality sources that adds interpretability, conferring validation and better 47 understanding of each case.

48 Introduction

49 Magnetic Resonance (MR) is widely used for non-invasive investigations of brain tumours, in particular 50 in vivo diagnosis and grading, surgical planning and assessment of response to therapy. It is generally 51 applied as MR imaging (MRI), see Fig 1(a), which provides a morphologic characterisation of tissues, 52 and it is the modality of choice in diagnosis, aggressiveness assessment and follow-up. However, there 53 are examples (i.e. malignant gliomas) where current imaging techniques lack diagnostic accuracy [1]. 54 In contrast, MR spectroscopy (MRS) provides biochemical information, resulting in a precise 55 metabolomic signature of the target tissue, which enables the identification of a wide array of molecules 56 present in tissues. MR spectroscopic imaging (MRSI), see Fig 1(b and c), produces a spatial distribution 57 of these metabolomic profiles, and thus delivers information about the spatial localisation of molecules [2,3]. Typically, an MRSI acquisition of the brain consists of a spectral grid of varying dimensions (e.g. 58 59 10-by-10, 12-by-12) superimposed on the image, covering only a part of the full image.

60

Fig 1. Two Magnetic Resonance approaches, MRI and MRSI, acquired in a murine glioblastoma model. a) Region of interest of the MRI. b) 10-by-10 MRSI grid of voxels, showing the metabolic composition of the tissue

at voxel level. c) MRSI grid superimposed on the MRI image. d) MRS example of the non-tumour area of this mouse, indicating the position of a number of relevant metabolites: choline (Cho), creatine (Cr) and N-acetyl aspartate (NAA). e) MRS example of the non-tumour area of this mouse, including lactate/mobile lipids (Lac/ML), and highlighting the changes that occur to these relevant metabolites.

Glioblastoma (GB) is the most frequent malignant intra-cranial tumour, having a very poor prognosis. Currently there is no cure for the disease. The standard treatment is surgery, with the aim of maximal safe tumour removal, followed by radio- and chemotherapy [4]. Despite this, due to the infiltrative nature of GB it is not always possible to assess the true degree of infiltration for a total tumour resection using conventional MRI [5]. Additionally, chemo- and radiotherapy only provide a small increase in the overall survival [6]. Eventually, most patients end up relapsing, and when this happens, they may be offered the possibility of starting with either second-line or experimental treatment approaches. One of the problems at this stage is the early assessment of progression using non-invasive methods such as MRI, which may be inaccurate for some patients (e.g. distinguishing true progression from pseudoprogression [7]). In this sense, non-invasive tools able to accurately distinguish the compromised area, which in turn would allow early prediction of relapse, would be of maximal benefit.

78 Pattern recognition and machine learning methods have been extensively applied to MR data of brain 79 tumours, to assist with different clinical issues, from diagnosis and prognosis of several pathologies, to 80 delineation of tumour masses [8–11]. Most studies have been performed on single-voxel MRS [12–16], 81 where a single spectrum is acquired from the pathological area. Even though substantial advances have 82 been achieved, there are still challenges from the methodological point of view that need to be 83 addressed. One of them is the ability to combine, in a principled manner, information from two different 84 MR approaches such as images and spectra. As can be seen in Fig 1, the resolution of the MRSI (i.e. 85 number of voxels of each acquisition) is considerably lower than the resolution of the MRI, which is at 86 the pixel level. This combination of MR images and spectra poses an important challenge, as it is 87 necessary to deal with different types of signals that also have different resolutions [17,18].

In biomedical research, animal (preclinical) models are useful for testing new drugs or treatments. One of the main advantages is the possibility of performing post-mortem studies – for example in the case of brain studies, to excise the whole brain and perform a detailed histopathological analysis. This allows the validation of imaging techniques and mathematical analyses or transformations of those, in contrast to patient studies, in which such validation approaches are not feasible due to obvious ethical restrictions.

The clinical value of a multivariate statistical analysis based on multiparametric MRI and MRSI for the non-invasive analysis of brain tumours has been previously assessed in a number of publications, such as [9,10,19]. They show that results combining MR approaches are more accurate and have superior diagnostic value compared with single approach. Most of those works used supervised mathematical models that explicitly require class information, i.e. tumour type and grade. This is often achieved in an *ad-hoc* manner by concatenating or mixing selected characteristics from each approach (that can be MR images and spectra), such as in [3,20,21]. A more recent study [22] makes use of Structured Data Fusion (SDF) [23], which could be potentially used for a more appropriate coupling of the information by joining the factors that are obtained in the factorisation process. However, authors in [22] do not seem to have used SDF in that way, but instead chose to concatenate the information as in the aforementioned studies. Providing multiparametric MRI and MRSI approaches in a principled manner may help to overcome the instability in the tissue segmentation that may arise from intrinsic mixing in data space.

106 Therefore, the purpose of our study was to develop a new methodology for embedding morphological 107 information from MR images into the MRSI analysis of brain tumours in animal models, using a Semi-108 Supervised approach to Source Extraction (SSSE). We applied this approach to retrospective MR data 109 from an orthotopic murine GB model (GL261 GB growing into C57/BL6 mice), widely used in 110 preclinical research, which mimics most of the human GB features [24]. In order to validate the 111 MRI+MRSI fusion, preclinical data allowed us to assess the quality of the tumour segmentation in 112 comparison to a third, independent technique (histopathology). We applied our methodology to both 113 control and treated tumour-bearing mice.

114 Materials and methods

115 Ethics Statement

No ethics approval was required for the current retrospective study. All studies with mice were approved previously by the local ethics committee [*Comissió d'Ètica en l'Experimentació Animal i Humana* (CEEAH). Available: <u>http://www.uab.cat/etica-recerca/</u>. Last accessed 29/06/2018], according to the regional and state legislation (protocol DARP-3255/CEEAH-530). Mice were periodically subjected to welfare inspections to check for any early symptoms of suffering and an objective scale for signs and symptoms was established. Mice were obtained from Charles River Laboratories (France) and housed at the animal facility of the *Universitat Autònoma de Barcelona (Servei d'Estabulari*).

123 MR studies

MR studies were carried out at the joint nuclear MR facility of UAB and CIBER-BBN, Unit 25 of NANBIOSIS (<u>www.nanbiosis.es</u>), with a 7 Tesla horizontal magnet (BioSpec 70/30, Bruker BioSpin, Ettlingen, Germany). Details of the acquisition parameters can be found in the Supporting Information file.

MRSI data were processed as described in [25,26]. The MRSI data grid was formed by an array of 10×10 voxels (MR spectrum from each voxel contained 692 data points), with an in-plane resolution of 0.55×0.55 mm and a 1 mm slice thickness in the 3rd dimension [25]. This volume of interest was manually positioned approximately in the centre of the brain, based on the reference image, in a way that it would include most of the tumour mass and also part of the normal/peritumoural brain parenchyma.

The study was performed on retrospective data already acquired. Only the spectral information (MRSI) from these data had been used in previous pattern recognition studies [25–28], performed for other purposes. Reference T2w MRI for all mice had not been used previously in any of the analyses, except for providing the anatomic overlay for the MRSI data. This is the first time that the images (MRI) were also part of the pattern recognition analysis for these mice.

139 **Datasets**

140 Pre-treatment data for analysis of tumour vs. non-tumour (groups A and B)

141 In this section, we describe the control (untreated) mice data that was used in this study to evaluate the 142 ability of SSSE to delineate the tumour mass. This data is summarised in Table 1 and includes:

A. MRI and MRSI (short TE, 12ms) data of six mice from [25]. The MRSI data in the mentioned
study had been used for the purpose of discriminating the tumour from the healthy tissue, in a
fully unsupervised way.

B. MRI and MRSI (short TE, 14 ms) data of five mice from [26,28]. The MRSI data in the
mentioned studies had been used as control (untreated) group to assess response to therapy, in
a semi-supervised way.

Follow-up, longitudinal data for analysis of tumour vs. non-tumour (group C)

151 In this section, we describe the follow-up, longitudinal data that was used in this study. This is data 152 obtained from mice under temozolomide (TMZ) treatment with the administration schedule described 153 in [28] and in the Supporting Information file.

The aim was to assess SSSE's ability to produce an accurate delineation of the tumour mass, as well as recognise the volume changes at different time points, and tumour response to therapy. This data is also summarised in Table 1 and includes:

- C. MRI and MRSI (short TE, 14 ms) data of two treated mice from [26]. Again, only the MRSI data had been used previously. For this study, we selected the two mice receiving treatment for the longest period from [26] (survival time of 45 and 34 days, and with 9 and 7 MR explorations, respectively).
- 161

162 **Table 1. Data used for analysis in this study.**

Group	Analysis in previous	References	Unique ID of mice (D: day post-	Number
	studies		inoculation)	of mice
А	Performed on untreated	[25,27]	C69 (D: 15), C71 (D: 16), C32 (D: 16),	6
	cases		C179 (D: 17), C233 (D: 17), C234 (D: 17)	
В	Performed on untreated	[26,28,29]	C255 (D: 14), C288 (D: 18), C520 (D: 18),	5
	cases		C529 (D: 18), C583 (D: 18)	
С	Performed on treated cases,	[26]	C819 (D: 10, 15, 18, 21, 25, 30, 33, 41,	2
	longitudinal study		45), C821 (D: 10, 15, 18, 21, 25, 30, 33)	

163 This table includes the references to original studies with this data, unique ID of animals, and their number of

164 individuals.

165 Histopathology

166 After the MRSI study (or at after MRSI endpoint in the Group C cases), the animals were euthanised 167 according to the ethics protocol by experienced personnel and the brains were collected and analysed 168 by histopathology as described in [28]. Caspase 3 immunohistochemical staining was used for detecting 169 apoptosis. Ki67 immunohistochemical staining was used to determine the spatial proliferating 170 population of cells in each tumour mass [25,30], calculated as a proliferation index (PI). In this 171 particular murine model, and according to the veterinary pathologist, PI > 30% would correspond to a 172 safe threshold for identifying the solid tumour region, whereas a PI \leq 5% would correspond to definitely non-tumour (excluding reactive gliosis and other phenomena). This is in agreement with other studies 173 with murine glioma, in which a PI of 23.9% was found in tumour core, and 9.6% in tumour periphery 174 175 [31].

The evaluation of necrosis was performed by the histopathologist on the haematoxylin and eosin stained slides. Different features were considered: isolated necrotic cells, moderate amounts of eosinophilic debris and large empty spaces. For each tumour, the percentage of the tissue section affected was semiquantified. When a tumour showed less than 20% of the mentioned necrotic features, a low grade of necrosis was assigned, while high grade of necrosis was assigned to those having more than 20% of the features. More details are included in [26].

Using all the available histopathological information such as Ki67 (which is information obtained *a posteriori*, or *ex-vivo*), the preclinical bioimaging expert produced a set of images with the aim of using them as the gold standard for this study. These images are compiled in Fig 2.

185

Fig 2. Delineation of the tumour area used as gold standard in this study. Images were produced *a posteriori* by the preclinical bioimaging expert for Groups A (first row), B (second row), and C (third and fourth rows). Two versions, (a) and (b), are available for C179, to study the main tumour mass first, and the two masses later, considering they have different proliferation indices, i.e. the rostral mass ("secondary mass") had a 5% $< PI \le 30$ while the caudal mass ("core mass") had a PI > 30%. Additionally, for C819 at day 41, a second (blue) area was
highlighted as abnormal.

192 Non-negative Matrix Factorisation for source extraction

193 In Non-negative Matrix Factorisation (NMF) methods [32,33] the non-negative data matrix X is 194 approximately factorised into two non-negative matrices: the matrix of sources or data basis S and the 195 mixing matrix H. The product of these two matrices provides an approximation to the original data 196 matrix in the form X \approx SH. There are different NMF variants, which mainly arise from using different 197 cost functions for computing the divergence between X and SH. While NMF describes the observed 198 data with positive-only mixtures of the latent variables or data sources, this does not apply to long echo 199 times where spectral phase-related signal modulation frequently results in negative values in the lactate 200 and alanine regions [12].

201 Convex Non-negative Matrix Factorisation (Convex-NMF) [34] is a variant of NMF that imposes a 202 restriction over the source matrix S to be a convex combination of the input data vectors. This restriction 203 significantly improves the quality of data representation of S. Unlike standard NMF, Convex-NMF 204 applies to both nonnegative and mixed-signed data matrices. What this means in practice is that: a) the 205 data are described by positive-only mixtures of the mixed-signed sources; and b) the sources, or latent 206 variables, are also positive-only mixtures of the data. This makes it easier to interpret both the mixing 207 and unmixing processes.

208 Semi-supervised methodology for source extraction in MRSI data

209 The semi-supervised methodology proposed in [13] involves three main stages and, in a nutshell, can210 be described as follows:

a) Definition of a Fisher Information (FI) metric to model pairwise similarities and dissimilarities
 between data points, using a Multi-Layer Perceptron (MLP) classifier to estimate the
 conditional probabilities of class membership.

214 b) Approximation of the empirical data distribution in a Euclidean projective space in which we 215 can apply NMF-based techniques. Multi-dimensional Scaling (MDS) is one of the algorithms proposed to do this mapping while retaining the distance structure generated by the FI matrix. 216 c) Application of Convex-NMF for the source decomposition of the data, which includes the 217 218 identification of the underlying sources and the calculation of the corresponding mixing matrix. 219 This semi-supervised methodology was previously applied to *single-voxel* data in [13], and *multi-voxel* 220 data in [26], although in a slightly different way. Both studies involved using the labels provided by 221 experts and combining spectra from different subjects to create a training dataset in which the sources 222 were extracted.

Proposed methodology to embed MRI information into the source

224 extraction

The proposed methodology, SSSE, builds upon the semi-supervised method proposed in [13] for the extraction of relevant sources, which guides the source extraction in the direction of provided class labels. In this new approach (see Fig 3), instead, we use the areas that arise from segmenting the MRI (i.e. T2w images), hence using the normal parenchyma/peritumoral/ventricle/tumour structures identified by MRI. We recommend this initial segmentation of the image to be performed manually by a researcher (e.g. radiologist, clinician, data analyst, etc.), but other automatic approaches can also be considered.

232

Fig 3. Diagram of SSSE. Details of the methodology proposed in this study for an extraction of sources in a semisupervised way, informed by knowledge hauled out from the T2w MRI.

Importantly, the semi-supervised nature of the proposed methodology has the benefit that it allows using only partial regions, so that areas of uncertainty can be left outside the initial segmentation, while allowing for concentration on the areas of maximum interest.

10

238 Following the initial selection of the areas of interest (or segmentation), we compute the posterior 239 probability of each class (or segmented region) for each pixel. As mentioned previously, our choice of 240 estimator of these probabilities, p(c|x), is a Multi-Layer Perceptron (MLP), which is a feed-forward artificial neural network. This is a semi-parametric non-linear probabilistic model of class membership, 241 242 for which a FI metric can be derived [35]. The parameters of the MLP were set as follows: We used one hidden layer of 6 nodes plus the output layer. The initial weights and bias were generated randomly 243 244 in the interval [-1, 1], the learning rate was set to 0.05, the momentum constant to 0.9, and weight decay 245 regularization was used to limit the size of the weights (lambda constant set to 0.01), which should 246 encourage the creation of simpler models with better generalisation capabilities. We sought model 247 convergence by allowing the MLP to iterate over a number of iterations (maximum epochs of 2000), 248 until the error was smaller than 5e-3. The models were trained using 75% of the instances for training 249 and the rest for test.

250 After calculating the posterior probability of each class for each pixel, as the resolution of the T2w image is higher than the one of the MRSI, we implement a voting system to bring the resolution of the 251 252 T2w image down to the spectroscopic imaging. Then, we train the neural network model using the 253 spectra from the MRSI and the labels provided by the segmentation, targeting the computed posterior probability of each class. From this point onwards, the rest of SSSE is similar to the semi-supervised 254 255 methodology proposed in [13], but applied intra-subject (i.e. to an individual mouse) as opposed to a 256 number of them (as in our previous study [13]). Final resulting maps with the produced segmentations 257 were linearly interpolated to bring them to the resolution of the image, as in [25].

It is important to stress that SSSE was designed to create a model of an individual case, as the purpose was to better understand and reflect the characteristics of each single patient. Hence, in order to avoid contamination from inter-subject overlaps, SSSE does not involve combining spectra from different subjects, thus focusing on intra-subject variation. What this means in practice is that every single case, C_i, was studied independently from the others (even excluding information from the same case acquired on a different day). From this data of case C_i, a proportion (detailed previously) was used for the initial training step as required by the methodology, and from there the rest of the proposed pipeline is unsupervised.

266 Evaluation of the results

267 To evaluate whether embedding information from the MRI into the data source extraction improves the quality of the tumour delineation, we compare SSSE segmentations with the ones obtained without 268 269 prior knowledge (Convex-NMF). We also compared SSSE with the approach proposed by Sauwen et 270 al. in [22], as they both bear some similarities in their aim to propose a semi-supervised / semi-271 automated method for the segmentation of brain tumours. For the latter comparison, some considerations had to be made to allow for a fair comparison of both methods (please see details in the 272 273 Supporting Information file). The three approaches will be tested against the gold standard (see Fig 2, and the Histopathology section for more details). 274

275 As measures used for comparison, we start by calculating the sensitivity and specificity of detecting the 276 tumour regions. The sensitivity, or true positive rate, is calculated as TP/(TP+FN), where true positive 277 (TP) are tumour pixels correctly labelled as tumours; and false negative (FN) are the tumour pixels 278 labelled as non-tumours. The specificity, or true negative rate, is calculated as TN/(TN+FP), where true 279 negative (TN) are the non-tumour pixels correctly identified as non-tumours, and false positive (FP) are 280 the non-tumour pixels labelled as tumours. A related measure frequently used in this area [36] for 281 comparing the similarity of two samples is the Dice score coefficient (DSC), also known as the 282 Sørensen–Dice coefficient [37], in order to show the effectiveness and robustness of proposed approach. 283 This is calculated from the values of TP, FP and FN, as follows:

$$DSC = \frac{2TP}{2TP + FP + FN} \tag{1}$$

As an overlap-based metric such as DSC can be dependent on the segmentation size, we also calculate two distance-based metrics: the Euclidean distance, and the Hausdorff distance. These distances were calculated between each of the resulting images and the corresponding one from the preclinical bioimaging expert, considered the gold standard in this study. The purpose was to determine how far (based on these distances) from the gold standard was the estimation of the tumour area when usingeach of the benchmarked approaches (i.e. Convex-NMF, Sauwen's and SSSE).

290 The Euclidean distance was calculated as in [38]. Hence, a pair of images E (estimated) and G (gold 291 standard) having feature vectors f^E and f^G , respectively, have the following distance:

Euc_dist(E,G) =
$$\sqrt{\sum_{i=1}^{n} (f_i^E - f_i^G)^2}$$
 (2)

Where n is the number of voxels in the images. The distance between two identical images is zero, i.e.
Euc_dist(G,G)=0; and the larger the value (distance), the bigger the difference between them.

Turning the distance measure into a shape similarity score that is easier to interpret, we calculated then the number of pixels that match values in the two images with reference to the total number of pixels, giving us a percentage of success.

The Hausdorff distance, in turn, measures how far two sets of points are from each other and was used here to measure the most mismatched tumour delineation between the three segmentations (Convex-NMF, Sauwen's and SSSE) with respect to the gold standard used. Let us consider B_E and B_G the boundaries of the tumour areas of the estimated and the gold standard images, respectively, of which we want to calculate the Hausdorff distance. It was then calculated as follows:

$$\text{Haus_dist}(B_{\text{E}}, B_{\text{G}}) = \max\left\{ \begin{array}{cc} \sup & \inf \\ e \in B_{\text{E}} \ g \in B_{\text{G}} \end{array} dist(e, g), \begin{array}{c} \sup & \inf \\ g \in B_{\text{G}} \ e \in B_{\text{E}} \end{array} dist(e, g) \right\}$$
(3)

302 where *sup* represents the supremum and *inf* the infimum. This distance will be zero if and only if B_E 303 and B_G have the same closure, i.e. both tumour areas are exactly the same.

- 304 Finally, the Kruskal-Wallis test was used to determine whether the results between the three approaches,
- 305 i.e. Convex-NMF, Sauwen's and SSSE, were statistically significant.

306 **Results**

The presentation of results is divided into two sections. Firstly, we show the results of applying SSSE to the mice in Groups A and B, which include untreated and treated cases, respectively; and to the mice in Group C, belonging to a longitudinal study with treated mice. (Please refer to Table 1 for more details and references to these groups). This is followed by the evaluation of the presented results at the end of this section.

312 Brain tumour delineation

Fig 4 shows that the sources obtained with the three approaches, for the different tissue types, are in some cases very similar to the naked eye, which is backed by correlations above 97% in most cases (e.g. comparing the red sources obtained with Convex-NMF, Sauwen's approach and SSSE). However, even when subtle in some cases, these small differences between them are reflected in their corresponding colour-coded maps, indicating the tumour delineation.

318

319 Fig 4. Results for the cases in Group A, for two classes.

320 For mouse C179, we also extracted three sources, in order to check whether a higher number of sources 321 could better represent its spatial heterogeneity – i.e. two tumour masses and three histologically 322 different regions with $PI \le 5\%$ (normal brain), $5\% < PI \le 30$ (secondary mass) and PI > 30% (core mass) 323 - see Fig 2. The results are presented in Fig 5. In this situation, both, the sources obtained and the 324 resulting maps, were more visually different. For example, when comparing the red source (representing 325 the main tumour mass) and the blue source (representing the non-tumour area) produced by SSSE with the equivalent sources produced by Convex-NMF, they showed high similarity between themselves 326 327 (with a correlation of 97% for the main tumour mass and 95% for the normal tissue). However, the yellow source obtained was less similar (with a correlation of 93%). More importantly, these two sets 328 329 of sources, i.e. red and yellow sources, were mainly representative of different areas of the brain, with 330 Sauwen's approach and SSSE providing a closer resemblance to the T2w image and the histopathological PI values of each mass (see Fig 2) than Convex-NMF. The latter uses mainly the red
source to represent both tumour masses, according to the preclinical bioimaging expert, and the yellow
source is covering both the solid tumour area and the non-tumour area.

334

Fig 5. Results for case C179 for three classes, from Group A.

Fig 6 shows the results obtained for the cases in Group B. These results were in line to those from Group A (excluding a few cases such as the three sources calculated for mouse C179), in the sense that the sources were not strikingly visually different, except for case C583, in which both the unsupervised tumour (red) and normal (blue) sources corresponded to patterns that matched with low signal-to-noise spectra. This is a problem that has been encountered and characterised before [39]. In the case of the non-tumour (blue) sources, they differed more than the tumour (red) source between the two approaches in all five mice.

343

344 Fig 6. Results for the cases in Group B, for two classes.

Fig 7 compiles the resulting colour maps (tumour delineation) after applying Convex-NMF, Sauwen's
approach and SSSE to the two mice in Group C, at the different time points studied.

347

Fig 7. Results for the cases in Group C, longitudinal study. Under each case there is a colour-bar showing the response stage determined by the RECIST criteria throughout the therapy protocol (orange means progressive disease, yellow stable disease and green partial response). At the bottom it is indicated when the three TMZ cycles were administered.

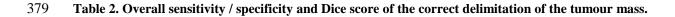
These colour-coded maps show how the volume of the tumour mass in each mouse changes as a result of their response to the three cycles of therapy. The RECIST criteria [40], which provides an indication of the response evaluation criteria in solid tumours, was determined for these two mice throughout the course of the treatment [26]. The adapted RECIST criteria were applied for mouse C819 [26] and in results from day 10 to day 18, the tumour was considered to be at the stage of progressive disease. At day 21, it entered the stable disease stage, remaining in a transient response state until day 25, when tumour shrinkage indicated partial response to the therapy. At days 30 and 33 the tumour was considered to be again in a stage of stable disease, gradually halting its response to the therapy and starting to regrow/relapse. Finally, at days 41 and 45 the tumour was considered again to be at the stage of progressive disease.

The adapted RECIST criteria for mouse C821 [26] indicated that the tumour was in the stage of progressive disease from day 10 to 21, in which the tumour grew from occupying ca. 15% of the area of the region of interest to nearly the 90% of it. This stage was followed by a short stable disease stage during days 30-35, followed again by another stage of progressive disease at the last day. A summarized explanation of the adapted RECIST criteria can be found in the Supporting Information file.

367 Evaluation of the tumour delineation against the gold standard

The results presented in the previous section for the three approaches were quantitatively evaluated using two main criteria: i) their ability to delineate the tumour regions (therefore discriminating the tumour from the non-tumour regions) with high sensitivity and specificity; and ii) their ability to produce colour-coded maps that are as close as possible to the gold standard (see Fig 2), which in this study, it is the set of images provided by the preclinical bioimaging expert (see more details in Histopathology and Evaluation of Results sections from Methods).

Details of the sensitivity and specificity values corresponding to the ability of each approach to detect the tumour masses can be found in Tables A in S1 File (for Groups A and B), B in S1 File (for more details on mouse C179 from Group A), and C in S1 File (for Group C). These tables also include the Dice score coefficient calculated for the three methods against the gold standard. A summary of these results is presented in Table 2.



Groups	Number	Sensitivity / Specificity		Dice score			
	of	Convex-	Sauwen et al.	SSSE	Convex-	Sauwen et	SSSE
	masses	NMF			NMF	al.	
A and B	1	0.90 ± 0.08 /	0.90 ± 0.08 /	0.94 ± 0.05 /	0.82 ± 0.11	0.84 ± 0.09	0.90 ± 0.05
		0.68 ± 0.23	0.76 ± 0.14	0.82 ± 0.16			
А	2	0.70 ± 0.42 /	0.87 ± 0.18 /	1.00 ± 0.00 /	0.45 ± 0.05	0.63 ± 0.13	0.82 ± 0.04
(C179)		0.68 ± 0.04	0.77 ± 0.11	0.88 ± 0.05			
С	1	0.88 ± 0.17 /	0.90 ± 0.08 /	0.94 ± 0.10	0.76 ± 0.13	0.82 ± 0.12	0.89 ± 0.10
		0.60 ± 0.17	0.72 ± 0.13	/ 0.81 ± 0.13			

380 Mean and standard deviation reported per group. First column indicates the group; second indicates the number 381 of tumour masses; third to fifth columns include the sensitivity / specificity results for the three approaches, 382 respectively; while sixth to eighth show their corresponding Dice scores. Shaded columns highlight the results 383 obtained with SSSE.

384

Next, we present the results of the Euclidean distance between each of the three methods to the gold standard, followed by a shape similarity score (see Evaluation of the results in the Methods section), and the Hausdorff distance between the same set of images. The results for the individual cases in Groups A and B are shown in Table S4; while the results for Group C can be seen in Table S5. A summary of them is presented in Table 3.

390	Table 3. Overall Euclidean distance / shape similarity score (%) and Hausdorff dista	nce.
-----	--	------

Groups	Number	Euclidean distance / Shape similarity score (%)			Hausdorff distance		
	of	Convex-NMF	Sauwen et al.	SSSE	Convex-	Sauwen et al.	SSSE
	masses				NMF		
A and B	1	99.72 ± 24.99 /	84.19 ± 14.46 /	73.88 ± 17.67	9.40 ± 1.35	8.22 ± 1.65	8.18 ± 1.49
		79.07 ± 11.62	85.72 ± 5.15	$/ 88.75 \pm 5.43$			
С	1	122.23 ± 34.23	102.41 ± 22.93	76.76 ± 27.32	10.22 ± 2.14	7.74 ± 1.80	6.61 ± 2.42
		/ 73.14 ± 14.52	/ 81.63 ± 7.57	/ 88.98 ± 8.18			

391 Distances between the produced colour-coded maps (Convex-NMF, Sauwen's and SSSE) and the expert's (mean 392 and standard deviation reported per group). Columns 1 and 2 as in Table 2. Third to fifth columns include the 393 Euclidean distance and the shape similarity score for the two approaches, respectively; while sixth to eighth show 394 their corresponding Hausdorff distance. Shaded columns highlight the results obtained with the proposed 395 methodology.

The results presented in Tables S4 and S5 were tested for significance (comparing the three approaches against each other) using a Kruskal-Wallis test, to decide whether the population distributions are identical (null hypothesis) without assuming them to follow the normal distribution. They resulted in a p-value < 0.00001 (any p-value < 0.05 is deemed as significant).

400 **Discussion**

401 This section mirrors the structure of the Results section, to facilitate the discussion.

402 Brain tumour delineation

403 Starting with a discussion of the tumour delineation results for mice in Groups A and B, we can see that 404 the high resemblance between the sources representing the same tissue type for each approach (Figs 4 405 to 6), is generally because the areas that they are representing are largely the same. However, the 406 seemingly small differences displayed between them have an important impact in the resulting colour-407 coded maps. This is not surprising as we have seen this effect in the past where very small differences 408 in the spectra led to the characterisation of the therapy response to temozolomide in preclinical 409 glioblastoma in [26]. In this study, SSSE achieved a sharper delimitation of the tumour masses when 410 comparing with Convex-NMF, probably due to the embedded information from the T2w image. 411 Additionally, it is worth mentioning that the inclusion of the MRI information did not affect the 412 biochemical interpretation of the sources, thanks to the way this information was embedded into the 413 model. Moreover, SSSE outperformed its counterpart approach proposed by Sauwen et al. when used 414 in equal conditions (i.e. same data), possibly because the initial information (labelling/segmentation) 415 fed into SSSE is preserving better the spatial configuration of the information.

416 Overall, for mice in Group A, SSSE and Sauwen's approach provided a more meaningful representation
417 than Convex-NMF. This is especially relevant for mouse C179. Metabolically, regarding the spectral

pattern represented, the yellow source obtained with Convex-NMF included metabolic features that
would be expected both in tumour and non-tumour areas, such as high mobile lipids and high NAA,
respectively. See relevant metabolites highlighted in Fig 1 d) and e).

421 In contrast, for mouse C179, SSSE yielded a source (coloured in yellow) that was very similar to the 422 red (tumour) source (Fig 5). The main difference between them was a higher peak signal from 423 lipids/lactate in the red source, which matched with the increased proliferation and necrosis, and the 424 higher choline to creatine ratio (3.21:3.03 ppm). The choline signal had the same intensity of the 425 lipid/lactate signal (1.28/1.33 ppm) in the yellow source, which is indicative of an active tumour, in 426 agreement with the intermediate proliferation indices that were recorded in the yellow region. This goes 427 in line to what we know about this case: this would be indeed expected, as the PIs calculated in zones 428 inside this secondary mass are indicative of tumour tissue, with PI values above 20%. This difference 429 in the spectral patterns are probably responsible for the production of the three coloured regions that 430 closely matched the three histologically different regions. In the case of Sauwen's approach, the obtained results are not too far from those obtained by SSSE, which reinforces the value of using any 431 available knowledge (in this case MRI information) from the case/patient to guide the source extraction 432 433 in a semi-automated/semi-supervised way.

434 Most importantly, in the case of Convex-NMF, when looking at the area in the colour-coded map that 435 this yellow source is representing (Fig 5), it is considerably far from the secondary tumour mass and it 436 is actually infiltrating non-tumour area in the bottom of the region of interest, which explains why this source exhibits some metabolic features of healthy tissue (see figure 11 available at [25]). The latter is 437 438 an important result as it shows that with both semi-supervised approaches, the system can be guided to 439 find a representation of the knowledge that the researchers would need modelling, giving them a tool 440 for testing different hypotheses – when left free in a completely unsupervised approach, the result will 441 not necessarily relate to anything of interest as they could be separating regions (e.g. artefacts, 442 ventricles, noise, etc.) that might not be relevant to the particular study.

The results for Group B show that, in general, the spectral pattern exhibited a great variation among
cases: for example, case C520, C529 and C583 show prominent peaks of lipids/lactate even in the non-

tumour region, whereas case C255 and C288 did not. This is not totally unexpected as the first three cases had larger tumour volumes than the other ones, with most voxels within the MRSI grid being represented either by the tumour itself or by the peritumoral infiltrating zone. Fig 8 shows a selection of voxels from one of these mice, i.e. C520, in which a high peak of lipids/lactate at c.a. 1.3 ppm can be seen, especially prominent in voxels a and b which could be due to tumour tissue infiltration.

450

451 Fig 8. MR spectra of three selected voxels from the non-tumour area.

However, even for the cases in which the similarities between the sources are higher, again the resulting maps were quite different, as seen in the results reported for the Group A. Regardless of this apparent high similarity, the colour maps show a different representation of the tumour areas for each approach, which are visually more coincident with the initial manual segmentation, but with the benefit that they also include the researcher-dubious (grey/uncertain) areas.

In addition to all the aspects mentioned before, both semi-supervised approaches have shown the ability to learn more meaningful, better-quality sources, as a way to overcome the susceptibility to the presence of artefacts and the lower signal-to-noise spectra issues reported in [39], with SSSE providing more accurate results according to the gold standard.

The delineation of the tumour area in the maps for the Group C show that, as observed for Groups A and B, SSSE results in more coincidental areas with the abnormal regions. Additionally, they are in accordance with the RECIST criteria for each of these images. Indeed, for both mice, there was a much higher correspondence between the RECIST criteria, and the maps obtained when using SSSE.

465 **Evaluation of the tumour delineation against the gold standard**

In most cases of Groups A and B, the sensitivity and specificity when using SSSE was better than the other two approaches (Tables 2 and A in S1 File), and in some cases by a large difference. The exceptions of a higher sensitivity with Convex-NMF and/or Sauwen's approach were seen in mice C179, C520 and C583, but these are at the cost of a much reduced specificity. If we look closer at mouse 470 C520, for example, we can see that it showed some atypical features around the ventricle which the imaging expert marked as abnormal, although this does not necessarily mean that it corresponds to core 471 tumour area, with PI > 30%. SSSE then benefitted from representing the tumour as a larger volume, but 472 473 failed to do it accurately, as can be seen with a drop in specificity. In the case of specificity, SSSE also 474 exhibited a better performance overall, only running aground with case C529 in which it also failed to 475 identify the abnormal features around the ventricle (see Fig S4, supporting information), as described 476 by the preclinical bioimaging expert, possibly because they are not part of the core tumour area with PI 477 > 30%.

When looking at the results of the analysis of the two abnormal masses from mouse C179 (see Fig 5 and Tables 2 and B in S1 File), we can see that in cases such as this one, semi-supervised approaches can make a huge difference when creating a model that represents areas of interest (notice that the resulting areas in the colour map, first row of Fig 5, do not represent such areas), with overall sensitivity and specificity of SSSE (1.00 and 0.88, respectively) outperforming Sauwen's approach (0.87 and 0.77, respectively) and Convex-NMF (0.70 and 0.68, respectively).

The sensitivity and specificity results for Group C are also consistent with the ones of Groups A and B.
A detailed discussion for this group can be found in the Supporting Information file (Discussion of the
tumour delineation sensitivity and specificity for Group C).

The Dice scores also show agreement with what was discussed previously. The semi-supervised approaches greatly outperform the unsupervised one, with SSSE exhibiting better performance. As recommended by Zijdenbos et al [41] in the literature of image validation, a good overlap occurs when DSC >0.70, which has been attained by the three approaches.

The Euclidean distance between the SSSE resulting maps and the gold standard were smaller in most of the cases than the distances between the maps obtained with the other two approaches and the gold standard (see Tables S4 and S5), which means that SSSE delineation of the tumour was more accurate than the other methods. There were only four exceptions to this (from all the 28 delineation maps produced in this study with the proposed methodology), two maps in group B, and another two in Group C. The ones in Group B were for mice C288 and C529, for which the Euclidean distances were slightly 497 worse for SSSE, however the Hausdorff distance for both cases indicated otherwise. In addition, our 498 proposed method did spot the anomaly in the ventricles of C529, which was also identified by the expert 499 pathologist when analysing the samples *a posteriori*. The exceptions in Group C were case C819 at day 41 and case C821 at day 21, in which the differences were marginal, and again the Hausdorff distances 501 contrarily show a better performance by SSSE. It is worth mentioning that the distance between two 502 images will indicate how much they differ, meaning that the shorter the distance between them the 503 higher their similarity.

Therefore, considering that a) most of the delineation maps produced by SSSE showed a notorious improvement over the unsupervised approach, and b) the maps produced by the counterpart, semisupervised approach proposed by Sauwen et al. did not generally outperform SSSE, we can confidently say that overall, the distance of the maps produced by SSSE to the gold standard were considerably shorter, meaning that SSSE was better suited for the problem and data at hand.

Previous results for the Euclidean distances between the three approaches to the gold standard harmonise with those obtained for the shape similarity score, as these two evaluation methods are highly related, except that the latter provides a better understanding and interpretability of what these distances mean. Overall, for Groups A and B, the proposed methodology exhibited an improvement over the unsupervised approach in the shape similarity score of nearly 10%; and Group C showed an improvement of more than 15% (both with a much smaller standard deviation).

The results presented in Tables S4 and S5 (referring to the Euclidean distance, similarity score, and Hausdorff distance between the three approaches to the gold standard) were tested for significance using a Kruskal-Wallis test, obtaining a p-value < 0.00001, which indicates that the difference between these approaches are statistically significant (as p < 0.05). Furthermore, statistically significant differences were found between the 28 delineation maps produced by the unsupervised approach and Sauwen's approach in comparison to the 28 produced by SSSE.

521 One final note goes to the fact that the proposed methodology does not combine MRI and MRSI 522 information by concatenation, nor it constrains the MRSI to fit the MRI segmentation, as opposed to 523 several previous works, such as [3,20–22]. Instead, our proposed methodology embeds the information 524 coming from the MRI (e.g. the manually selected areas) into the analysis of the MRSI by guiding the source extraction (which are MR spectra) in the direction of the areas of interest, according to the MR 525 image. Our reason to avoid direct concatenation of the information from these MR approaches was to 526 propose a model able to integrate them in a principled manner. Moreover, we use the full MR spectra 527 528 in the usual range of interest [4.5 - 0 ppm], as opposed to quantifying only a selection of metabolites 529 as in [3.20,21]. The added value of the latter is interpretability, providing not only the visualisation of 530 the resulting map with the delineation of the tumour areas and healthy parenchyma, but also the spectral 531 pattern associated to each of these segmented regions. This allows for extra validation and reassurance, 532 and more importantly, better understanding of the results.

533 **Conclusions**

534 Overall, the quality of the resulting colour-coded maps indicating the tumour delineation with the 535 proposed methodology was considerably better than when using only Convex-NMF in a completely 536 unsupervised approach, as in [25], or even an alternative semi-supervised approach proposed by Sauwen et al. [22]. This was carefully assessed in a quantitative way, showing that, in most cases, the 537 538 sensitivity and specificity of delineating the tumour masses (which provide a measure of accuracy and 539 confidence in these delineations) was far superior when using the proposed methodology, SSSE. These 540 results were also consistent with the shape similarity scores and distances calculated for both sets of images (in both approaches) to the gold standard (images from the imaging expert), which can be 541 542 considered statistically significant.

These results also come with additional advantages, namely: a) the proposed methodology is able to effectively deal with signal-to-noise issues, which is not the case of the unsupervised approach in [25]; b) it allows radiologists/clinicians to define the area of interest to them and, with that, guide the process of source extraction, which was not a possibility in [25]; c) while still creating an intra-subject model, as opposed to [26] where the model was trained using a set of subjects, therefore needing to deal with the tumour heterogeneity of GB, which is a well-recognised problem [42], and d) in addition to a segmented images, SSSE also produce meaningful, good-quality sources that represent each of the regions of interest, which adds an extra layer of interpretability to the results obtained, conferring not only validation of the results, but also better understanding and analysis of each individual case.

Therefore, given the quality of the obtained results, and the advantages identified in the use of the proposed methodology, we consider that the extra pre-processing steps related to the embedding of the MRI information into the MRSI data source extraction are worthwhile, as they have shown to improve the tumour delineation in the preclinical GB model. Once again, the multiparametric character of the proposed approach (fusing MRI and MRSI) has shown to provide better results compared with using a single approach (MRSI) [26].

558 Abbreviations

FI: Fisher Information. GB: Glioblastoma. MDS: Multi-dimensional Scaling. MLP: Multi-Layer
Perceptron. MR: Magnetic Resonance. MRI: Magnetic Resonance Imaging. MRS: MR spectroscopy.
MRSI: Magnetic Resonance Spectroscopic Imaging. NMF: Non-negative Matrix Factorisation. PI:
proliferation index. RECIST: response evaluation criteria in solid tumours. SSSE: semi-supervised
source extraction. T2w: T2-weighted.

564 Authors' contributions

SOM and IO conceived and designed the study. SOM implemented the methods and carried out the experiments. PR assisted with the experiments carried out with Sauwen et al. approach. APC performed the initial manual segmentations of mice from studies B and C. APC and MJS provided the data and interpretations to the results. RT and PR assisted with the evaluation of the results. SOM, IO, PR, APC and MSJ helped to draft the manuscript. All authors read and approved the final version of it.

570 **References**

Julià-Sapé M, Acosta D, Majós C, Moreno-Torres A, Wesseling P, Acebes JJ, et al. Comparison
 between neuroimaging classifications and histopathological diagnoses using an international

573		multicenter brain tumor magnetic resonance imaging database. J Neurosurg. 2006;105: 6–14.
574	2.	Segebarth CM, Balériaux DF, Luyten PR, Den Hollander JA. Detection of metabolic
575		heterogeneity of human intracranial tumors in vivo by 1H NMR spectroscopic imaging. Magn

576 Reson Med. 1990;13: 62–76.

- Luts J, Laudadio T, Idema AJ, Simonetti AW, Heerschap A, Vandermeulen D, et al. Nosologic
 imaging of the brain: segmentation and classification using MRI and MRSI. NMR Biomed.
 2009;22: 374–390. doi:10.1002/nbm.1347
- Wen PY, Macdonald DR, Reardon DA, Cloughesy TF, Sorensen AG, Galanis E, et al. Updated
 response assessment criteria for high-grade gliomas: response assessment in neuro-oncology
 working group. J Clin Oncol. 2010;28: 1963–72. doi:10.1200/JCO.2009.26.3541
- 5. Widhalm G, Minchev G, Woehrer A, Preusser M, Kiesel B, Furtner J, et al. Strong 5aminolevulinic acid-induced fluorescence is a novel intraoperative marker for representative
 tissue samples in stereotactic brain tumor biopsies. Neurosurg Rev. 2012;35: 381–391.
 doi:10.1007/s10143-012-0374-5

Stupp R, Mason WP, van den Bent MJ, Weller M, Fisher B, Taphoorn MJB, et al. Radiotherapy
 plus Concomitant and Adjuvant Temozolomide for Glioblastoma. N Engl J Med. 2005;352(10):
 987–996.

- 590 7. Brandes AA, Tosoni A, Spagnolli F, Frezza G, Leonardi M, Calbucci F, et al. Disease
 591 progression or pseudoprogression after concomitant radiochemotherapy treatment: pitfalls in
 592 neurooncology. Neuro Oncol. 2008;10: 361–7. doi:10.1215/15228517-2008-008
- Ortega-Martorell S, Julià-Sapé M, Lisboa P, Arús C. Pattern Recognition Analysis of MR
 Spectra. eMagRes. Chichester, UK: John Wiley & Sons, Ltd; 2016. pp. 945–958.
 doi:10.1002/9780470034590.emrstm1484
- De Edelenyi FS, Rubin C, Estève F, Grand S, Décorps M, Lefournier V, et al. A new approach
 for analyzing proton magnetic resonance spectroscopic images of brain tumors: nosologic
 images. Nat Med. 2000;6: 1287–1289.

- 599 10. Simonetti AW, Melssen WJ, van der Graaf M, Postma GJ, Heerschap A, Buydens LMC. A
 600 Chemometric Approach for Brain Tumor Classification Using Magnetic Resonance Imaging
 601 and Spectroscopy. Anal Chem. 2003;75: 5352–5361.
- Ortega-Martorell S, Vellido A, Lisboa PJG, Julià-Sapé M, Arús C. Spectral decomposition
 methods for the analysis of MRS information from human brain tumors. International Joint
 Conference on Neural Networks (IJCNN 2011), Proceedings. San José, California, USA; 2011.
 pp. 3279–3284.
- 606 12. Ortega-Martorell S, Lisboa PJG, Vellido A, Julià-Sapé M, Arús C. Non-negative Matrix
 607 Factorisation methods for the spectral decomposition of MRS data from human brain tumours.
 608 BMC Bioinformatics. 2012;13.
- Ortega-Martorell S, Ruiz H, Vellido A, Olier I, Romero E, Julià-Sapé M, et al. A Novel SemiSupervised Methodology for Extracting Tumor Type-Specific MRS Sources in Human Brain
 Data. PLoS One. 2013;8: e83773. doi:10.1371/journal.pone.0083773
- 612 14. Ortega-Martorell S, Olier I, Julià-Sapé M, Arús C. SpectraClassifier 1.0: a user friendly,
 613 automated MRS-based classifier-development system. BMC Bioinformatics. 2010;11: 106.
- 614 15. García-Gómez JM, Luts J, Julià-Sapé M, Krooshof P, Tortajada S, Robledo J, et al. Multiproject615 multicenter evaluation of automatic brain tumor classification by magnetic resonance
 616 spectroscopy. Magn Reson Mater Physics, Biol Med. 2009;22: 5–18.
- 617 16. García-Gómez JM, Tortajada S, Vidal C, Juliá-Sapè M, Luts J, Moreno-Torres A, et al. The
 618 effect of combining two echo times in automatic brain tumor classification by MRS. NMR
 619 Biomed. 2008;21: 1112–1125.
- De Vos M, Laudadio T, Simonetti A, Heerschap A, Van Huffel S. Fast nosologic imaging of the
 brain. J Magn Reson. 2007;184: 292–301.
- 18. Sauwen N, Acou M, Van Cauter S, Sima DM, Veraart J, Maes F, et al. Comparison of
 unsupervised classification methods for brain tumor segmentation using multi-parametric MRI.
 NeuroImage Clin. 2016;12: 753–764. doi:10.1016/j.nicl.2016.09.021

- Postma GJ, Luts J, Idema AJ, Julià-Sapé M, Moreno-Torres Á, Gajewicz W, et al. On the 625 19. relevance of automatically selected single-voxel MRS and multimodal MRI and MRSI features 626 brain 627 for tumour differentiation. Comput Biol Med. 2011:41: 87-97. doi:10.1016/j.compbiomed.2010.12.003 628
- Sauwen N, Sima DM, Van Cauter S, Veraart J, Leemans A, Maes F, et al. Hierarchical nonnegative matrix factorization to characterize brain tumor heterogeneity using multi-parametric
 MRI. NMR Biomed. 2015;28: 1599–1624. doi:10.1002/nbm.3413
- Li Y, Liu X, Wei F, Sima DM, Van Cauter S, Himmelreich U, et al. An advanced MRI and
 MRSI data fusion scheme for enhancing unsupervised brain tumor differentiation. Comput Biol
 Med. 2017;81: 121–129. doi:10.1016/J.COMPBIOMED.2016.12.017
- Sauwen N, Acou M, Sima DM, Veraart J, Maes F, Himmelreich U, et al. Semi-automated brain
 tumor segmentation on multi-parametric MRI using regularized non-negative matrix
 factorization. BMC Med Imaging. 2017;17: 29. doi:10.1186/s12880-017-0198-4
- 638 23. Sorber L, Van Barel M, De Lathauwer L. Structured Data Fusion. IEEE J Sel Top Signal
 639 Process. 2015;9: 586–600. doi:10.1109/JSTSP.2015.2400415
- Cha S, Johnson G, Wadghiri YZ, Jin O, Babb J, Zagzag D, et al. Dynamic, contrast-enhanced
 perfusion MRI in mouse gliomas: Correlation with histopathology. Magn Reson Med. 2003;
 doi:10.1002/mrm.10446
- 643 25. Ortega-Martorell S, Lisboa PJG, Simões R V, Pumarola M, Julià-Sapé M, Arús C. Convex Non644 Negative Matrix Factorization for brain tumor delimitation from MRSI data. PLoS One. 2012;7:
 645 e47824.
- Delgado-Goñi T, Ortega-Martorell S, Ciezka M, Olier I, Candiota AP, Julià-Sapé M, et al.
 MRSI-based molecular imaging of therapy response to temozolomide in preclinical
 glioblastoma using source analysis. NMR Biomed. 2016;29: 732–743. doi:10.1002/nbm.3521
- 649 27. Simões R V., Delgado-Goñi T, Lope-Piedrafita S, Arús C. 1H-MRSI pattern perturbation in a
 650 mouse glioma: the effects of acute hyperglycemia and moderate hypothermia. NMR Biomed.

651 2010;23: 23–33. doi:10.1002/nbm.1421

- Delgado-Goñi T, Julià-Sapé M, Candiota AP, Pumarola M, Arús C. Molecular imaging coupled
 to pattern recognition distinguishes response to temozolomide in preclinical glioblastoma. NMR
 Biomed. 2014;27: 1333–1345. doi:10.1002/nbm.3194
- 655 29. Ortega-Martorell S, Olier I, Delgado-Goñi T, Ciezka M, Julià-Sapé M, Lisboa P, et al. Semi-
- 656 supervised source extraction methodology for the nosological imaging of glioblastoma response
- to therapy. 2014 IEEE Symposium on Computational Intelligence and Data Mining,
 Proceedings. 2015. pp. 93–98. doi:10.1109/CIDM.2014.7008653
- 30. Ostertag CB, Volk B, Shibata T, Burger P, Kleihues P. The monoclonal antibody Ki-67 as a
 marker for proliferating cells in stereotactic biopsies of brain tumours. Acta Neurochir (Wien).
 1987;89: 117–121.
- Wang T-C, Cheng C-Y, Yang W-H, Chen W-C, Chang P-J. Characterization of highly
 proliferative secondary tumor clusters along host blood vessels in malignant glioma. Mol Med
 Rep. 2015;12: 6435–6444. doi:10.3892/mmr.2015.4228
- Beatero P, Tapper U. Positive matrix factorization: A non-negative factor model with optimal
 utilization of error estimates of data values. Environmetrics. 1994;5: 111–126.
- 667 33. Lee DD, Seung HS. Learning the parts of objects by non-negative matrix factorization. Nature.
 668 1999;401: 788–791.
- 669 34. Ding C, Li T, Jordan MI. Convex and semi-nonnegative matrix factorizations. IEEE Trans
 670 Pattern Anal Mach Intell. 2010;32: 45–55.
- 671 35. Ruiz H, Jarman IH, Martín JD, Lisboa PJG. The role of Fisher information in primary data space
 672 for neighbourhood mapping. European Symposium on Artificial Neural Networks,
 673 Computational Intelligence and Machine Learning (ESANN). Bruges, Belgium; 2011. pp. 381–
 674 6.
- 675 36. Zou KH, Warfield SK, Bharatha A, Tempany CMC, Kaus MR, Haker SJ, et al. Statistical

- 676 Validation of Image Segmentation Quality Based on a Spatial Overlap Index. Acad Radiol.
 677 2004;11: 178–189. doi:10.1016/S1076-6332(03)00671-8
- 678 37. Dice LR. Measures of the Amount of Ecologic Association Between Species. Ecology. 1945;
 679 doi:10.2307/1932409
- Safar MH, Shahabi C. Image Similarity Measures. In: Shape Analysis and Retrieval of
 Multimedia Objects. Multimed Syst Appl. 2003;23: 9–11. doi:10.1007/978-1-4615-0349-1 2
- Mocioiu V, Kyathanahally SP, Arús C, Vellido A, Julià-Sapé M. Automated Quality Control for
 Proton Magnetic Resonance Spectroscopy Data Using Convex Non-negative Matrix
 Factorization. Bioinformatics and Biomedical Engineering Proceedings of IWBBIO 2016.
 Granada, Spain: Springer; 2016. pp. 719–727. doi:10.1007/978-3-319-31744-1_62
- 40. Eisenhauer EA, Therasse P, Bogaerts J, Schwartz LH, Sargent D, Ford R, et al. New response
 evaluation criteria in solid tumours: Revised RECIST guideline (version 1.1). Eur J Cancer.
 2009;45: 228–247. doi:10.1016/j.ejca.2008.10.026
- 41. Zijdenbos AP, Dawant BM, Margolin RA, Palmer AC. Morphometric Analysis of White Matter
 Lesions in MR Images: Method and Validation. IEEE Trans Med Imaging. 1994;
 doi:10.1109/42.363096
- 42. Sottoriva A, Spiteri I, Piccirillo SGM, Touloumis A, Collins VP, Marioni JC, et al. Intratumor
 heterogeneity in human glioblastoma reflects cancer evolutionary dynamics. Proc Natl Acad Sci
 U S A. 2013;110: 4009–4014. doi:10.1073/pnas.1219747110

695

696 Supporting Information

697 S1 File. Supporting Information: Embedding MRI information into MRSI data source extraction
 698 improves brain tumour delineation in animal models. This document includes additional
 699 information regarding the Magnetic Resonance studies, TMZ administration and preparation, how

- 700 Sauwen et al. method was used, how the initial segmentation was performed, and further details on the
- 701 evaluation and discussion of the results.